Electron dynamics in the minimagnetosphere above a lunar magnetic anomaly

Usui, Hideyuki
Miyake, Yohei
Nishino, Masaki N.
Matsubara, Takuma
Wang, Joseph

(Citation)
Journal of Geophysical Research: Space Physics,122(2):1555-1571

(Issue Date)
2017-02

(Resource Type)
journal article

(Version)
Version of Record

AGU PUBLICATIONS

JGR

Journal of Geophysical Research: Space Physics

RESEARCH ARTICLE

10.1002/2016JA022927

Electron dynamics in the minimagnetosphere above a lunar magnetic anomaly

Hideyuki Usui[1], Yohei Miyake[2], Masaki N. Nishino[3], Takuma Matsubara[1], and Joseph Wang[4]

[1]Graduate School of System Informatics, Kobe University, Kobe, Japan, [2]Education Center on Computational Science and Engineering, Kobe University, Kobe, Japan, [3]Institute for Space-Earth Environment Research, Nagoya University, Nagoya, Japan, [4]Department of Astronautical Engineering, University of Southern California, Los Angeles, California, USA

Key Points:
- The electron current dominates the boundary layer of a minimagnetosphere above a lunar magnetic anomaly
- Electron boundary current shows two symmetric structures in which the convection reverses direction with respect to the magnetic equator
- Electrons in the innermost boundary layer obtain maximum velocity due to the acceleration by the electric field due to charge separation

Correspondence to:
H. Usui,
h-usui@port.kobe-u.ac.jp

Citation:
Usui, H., Y. Miyake, M. N. Nishino, T. Matsubara, and J. Wang (2017), Electron dynamics in the min-imagnetosphere above a lunar magnetic anomaly, *J. Geophys. Res. Space Physics*, *122*, 1555–1571, doi:10.1002/2016JA022927.

Received 10 MAY 2016
Accepted 20 JAN 2017
Accepted article online 25 JAN 2017
Published online 3 FEB 2017

Abstract We consider a three-dimensional electromagnetic particle-in-cell simulation of the boundary layer current in a minimagnetosphere created by the interaction between a magnetized plasma flow, which models the typical solar wind, and a small-scale magnetic dipole, which represents the Reiner Gamma magnetic anomaly on the lunar surface. The size of this magnetic anomaly (measured as the distance from the dipole center to the position where the pressure of the local magnetic field equals the dynamic pressure of the solar wind) is one quarter that of the Larmor radius of the solar wind ions. In spite of the weak magnetization of the ions, a minimagnetosphere is formed above the magnetic anomaly. In the boundary layer of the minimagnetosphere, the electron current is dominant. Due to the intense electric field induced by charge separation, electrons entering the boundary layer undergo $\boldsymbol{E} \times \boldsymbol{B}$ drift. In each hemisphere, the electron boundary current due to the drift shows a structure where the convection reverses; these structures are symmetric with respect to the magnetic equator. Detailed analysis of the electron cyclotron motion shows that electrons at the edge of the inner boundary layer obtain maximum velocity by the electric field acceleration due to the charge separation, not due to the drift of the electron's guiding center. The maximum electron velocity is approximately 8 times that of the upstream plasma. The width of the boundary layer current becomes approximately equal to the radius of the local electron cyclotron.

1. Introduction

The lunar plasma environment has been investigated intensively by recent spacecraft, such as KAGUYA [e.g., *Saito et al.*, 2008, 2010, 2012] and Chandrayaan-1 [e.g., *Barabash et al.*, 2009; *Bhardwaj et al.*, 2010]. In addition to macroscopic plasma structures, such as the wake structure formed in the downstream region, small-scale perturbations of plasma distribution and fields have been observed in the dayside region, mostly over the crustal magnetic anomalies found on the lunar surface. The KAGUYA spacecraft observed more than 10% of the solar wind protons reflected at an altitude of approximately 100 km over the magnetic anomalies [*Saito et al.*, 2010]. Chandrayaan-1 determined that the deflection of the solar wind protons was highly efficient (greater than 10%) [*Lue et al.*, 2011], and it also observed backstreaming hydrogen atoms over the magnetic anomalies [*Wieser et al.*, 2010]. It was also found that plasma wave activities were enhanced over the magnetic anomalies [e.g., *Halekas et al.*, 2006; *Hashimoto et al.*, 2010]. These observations suggest that the plasma and field disturbances over the magnetic anomalies are caused by interactions of the solar wind with the local magnetic field. Unlike the Earth's magnetosphere, the dipole moment of the lunar magnetic anomalies is very weak, and the resulting dipole field region is much smaller than the characteristic spatial scales of the solar wind, such as the inertial length and Larmor radius r_{iL} of the ions in the interplanetary magnetic\bgroup \egroup field (IMF).

When the direction of the solar wind is orthogonal to the dipole moment M, we can characterize the size of the region affected by the magnetic dipole immersed in the solar wind by a distance L from the dipole center to the upstream position at which the pressure of the local magnetic field equals the dynamic pressure of the solar wind at the magnetic equator. We use the magnetohydrodynamics (MHD) approximation for L. To derive L, we use the following formulation for a dipole magnetic field in free space:

$$\boldsymbol{B} = \frac{\mu_0}{4\pi}\left(\frac{3(\boldsymbol{M}\cdot\boldsymbol{r})\boldsymbol{r}}{r^5} - \frac{\boldsymbol{M}}{r^3}\right) \quad (1)$$

where $\boldsymbol{r}$ is the position vector with respect to the dipole center, and μ_0 is the permeability in a vacuum. When $\boldsymbol{M}$ is set to be perpendicular to the solar wind, we can obtain the intensity of the dipole field $|B|$ from equation (1) as a function of the intensity of the magnetic moment $|M|$ and the upstream position x from the dipole center along the sunward direction:

$$|B| = \frac{\mu_0 |M|}{4\pi x^3} \tag{2}$$

By setting $x = L$ in the above equation, we can calculate $|B|$ for the location at which the magnetic pressure equals the dynamic pressure of the solar wind. Then, L is obtained as follows (as shown in *Ashida et al.* [2014]):

$$L = \left(\frac{\mu_0 M^2}{16\pi^2 m_i n_0 v_{flow}^2} \right)^{\frac{1}{6}} \tag{3}$$

where n_0 and v_{flow} are the density and velocity of the plasma flow, respectively, and m_i is the ion mass. For lunar magnetic anomalies, L is less than or equal to 100 km, which is smaller than r_{iL}. In such a situation, the protons are almost unmagnetized, and their dynamics are not affected significantly by the local field of magnetic anomalies. However, as stated above, a variety of related phenomena, such as the reflection and deflection of ions, have been observed. Above magnetic anomalies, the mechanism underlying the ion dynamics is thought to be due to the interactions of the solar wind with those anomalies.

The interactions between a plasma flow and a small-scale magnetic dipole have been examined in various situations. The mesoscale is the region in which L is less than or comparable to r_{iL} but larger than the electron Larmor radius r_{eL}. In a feasibility study of a magnetosail [e.g., *Winglee et al.*, 2000] proposed for an interplanetary flight system, two-dimensional particle-in-cell (PIC) plasma simulations were used to examine the interactions of the solar wind with the mesoscale magnetic dipole that was artificially created by the superconducting coil on the spacecraft [*Moritaka et al.*, 2012]. That study showed the formation of a magnetosphere even in the mesoscale regime. In interactions between the solar wind and a mesoscale magnetic dipole, the electrons are magnetized, but the magnetization of the ions is weak at the magnetopause. An electric field is induced in the dayside magnetosphere as charges are separated due to the difference between the momentum of the electrons and that of the ions. It was shown that the electric field induced at the magnetopause can affect the dynamics of the incoming solar wind ions, and some of the ions can be reflected back in the sunward direction.

A similar interaction takes place between the solar wind and lunar magnetic anomalies. A minimagnetosphere with a density cavity has been studied both by spacecraft observations and by numerical simulations [e.g., *Harnett and Winglee*, 2000, 2003; *Halekas et al.*, 2008; *Bamford et al.*, 2012]. The plasma responses to the induced electric field have also been examined by conducting particle simulations [e.g., *Harnett and Winglee*, 2002; *Kallio et al.*, 2012; *Poppe et al.*, 2012; *Deca et al.*, 2014, 2015]. Laboratory experiments of plasma interactions with a small-scale magnetic dipole were also conducted, and the electric field induced by the interaction between a plasma flow and the local magnetic field has been examined [e.g., *Howes et al.*, 2015; *Jarvinen et al.*, 2014; *Wang et al.*, 2013; *Bamford et al.*, 2012]. The interaction of the solar wind with a magnetic anomaly was also examined using a hybrid particle simulation that used an empirical model of the Gerasimovich magnetic anomaly, which was based on observations of the Lunar Prospector [*Fatemi et al.*, 2015].

As has been pointed out in many previous studies, plasma kinetics, such as the finite Larmor radius effect, should be included when modeling the interactions between the solar wind and magnetic anomalies because L is almost the same as or smaller than r_{iL}. The electric field generated by charge separation at the magnetopause affects the dynamics of the solar wind ions and causes their reflection and deflection. Meanwhile, the solar wind electrons are magnetized in the minimagnetosphere. Hence, the boundary layer current is mainly due to the electron flux. It has been reported that the motion of electrons in the boundary layer is primarily $\boldsymbol{E} \times \boldsymbol{B}$ drift. The velocity distribution function of electrons at different locations above the magnetic anomaly were examined in *Deca et al.* [2015]. However, the details of the three-dimensional structure of the boundary layer current, which is dominated by the electron flux, have not been determined. In addition, the microscopic dynamics of electrons in the boundary layer has not been examined, nor has the electron cyclotron motion (ECM).

In this study, we use three-dimensional electromagnetic particle-in-cell simulations to investigate the spatial structure of the boundary layer current in a minimagnetosphere formed above a lunar magnetic anomaly.

Table 1. Parameters of the Solar Wind and the Magnetic Dipole of the Reiner Gamma Anomaly

	Notations	Typical Values
Parameters of the Solar Wind		
Density	n_e, n_i	3.5×10^6 m^{-3}
Flow velocity	v_{flow}	400 km/s
Mach number	Ma_A	10.0
Beta	β	0.96
Plasma temperature	T_e, T_i	8.6 eV
Ratio between electron cyclotron frequency and plasma frequency	Ω_{ce}/ω_{pe}	5.83×10^{-3}
Uniform magnetic field density	B_0	3.5 nT
Parameters of Reiner Gamma		
Latitude and longitude		7.5°N, 58.4°W
Inclination from the horizontal plane		1.3°
Magnetic moment	M	1.13×10^{13} Am^2
Distance between the dipole center and the lunar surface	$L_{surface}$	11 km

We focus on the electron dynamics in the boundary layer. In section 2, we describe the simulation method, model, and parameters used in this study. To examine the interactions between the solar wind and the Reiner Gamma magnetic anomaly, we used a magnetized plasma flow and a small-scale magnetic dipole; the plasma flow was perpendicular to the lunar surface, and the magnetic dipole was perpendicular to the direction of plasma flow. For the magnetic anomaly in our simulation, we let $r_{iL}/L = 4$. In section 3, we show the spatial variation of the plasma density and the current density by cutting different planes in the three-dimensional space obtained by the simulations. In addition to the density profiles of the minimagnetosphere created by the above magnetic anomaly, we also examine the three-dimensional structure of the boundary layer current. In section 4, we consider in detail the electron dynamics on the magnetic equator, particularly at the innermost edge of the boundary layer of the minimagnetosphere, where the electron density decreases to 0. We summarize our results and present our conclusions in section 5.

2. Simulation Methods, Model, and Parameters

This study is based on three-dimensional, full kinetic, electromagnetic particle-in-cell (EM-PIC) simulations. The basic numerical procedures used in the EM-PIC simulation are described in *Birdsall and Langdon* [1991]. In a PIC simulation, both ions and electrons are treated as particles in order to include the kinetic effects of the plasma particles, such as the finite Larmor radius and the charge separation between the different species of particles. To trace the motions, the equation of motion is solved for individual particles of both species. By using the updated velocity and position of the particles, the charge conservation method is used to calculate the current density at each spatial grid point; this method is based on the continuity equation for the charged particles [*Villasenor and Buneman*, 1992]. To calculate the evolution of electromagnetic fields in the simulation domain, Maxwell's equations are solved at each time step by using the finite difference time domain method. In Maxwell's equations, plasma dynamics are taken into account through the current density obtained at each grid point.

Table 1 shows typical solar wind parameters, which we used to model the upstream plasma, and the parameters we used for the Reiner Gamma magnetic anomaly. As reported in *Kurata et al.* [2005], the Reiner Gamma magnetic anomaly is typical of those found on the lunar surface; it is modeled as two magnetic dipoles, the southwest dipole (SW) and the northeast dipole (NE). In this study, we focus on SW, which has a dipole moment that is slightly inclined from the horizontal plane. Because it is located at a low latitude, we can assume that the magnetic dipole moment is almost parallel to the lunar surface and that it is perpendicular to the sunward direction.

In Table 2, we list the simulation parameters used in this study. For the plasma flow representing the solar wind, instead of using the actual measured physical values listed in Table 1, we scaled them to reduce the calculation time. We set the mass ratio between ions and electrons in the plasma flow to be $m_i/m_e = 100$, which allows us to clearly separate the dynamics of the two species of particles. We set the ratio of the speed

Table 2. Simulation Parameters

Parameters	Notations	Values
Mass ratio between ion and electron	m_i/m_e	100
Flow velocity	v_{flow}	$0.05v_c$
Mach number	Ma_A	5.0
Electron thermal velocity	v_{the}	$2.4v_{flow}$
Ion thermal velocity	v_{thi}	$0.24v_{flow}$
Ratio between electron cyclotron frequency and plasma frequency	Ω_{ce}/ω_{pe}	0.1
Grid size	dr	$1.0\lambda_D$
Time step	dt	$0.285dr/v_c$
Numbers of grids in the physical region	$N_x \times N_y \times N_z$	$192 \times 192 \times 192$
System dimensions	$l_x \times l_y \times l_z$	$5.6L \times 5.6L \times 5.6L$
Depth of the dipole moment under the lunar surface	L_{dipole}	$0.2L$
Ratio between the ion Larmor radius and L	r_{iL}/L	4

of light v_c to v_{flow} to be 20, although the actual ratio is about 600. The plasma flow is isothermal, and the ratio of the electron thermal velocity v_{the} to v_{flow} was set to be 2.4, which is almost the same as the actual ratio for the solar wind electrons. The ion thermal velocity v_{thi} was set to $0.24v_{flow}$. We used a static magnetic field B_0 to represent the IMF. The Alfvénic Mach number Ma_A, which is the ratio of v_{flow} to the Alfvén velocity v_A, was 5. For the solar wind, the beta value was set to unity, and the ratio of the electron cyclotron frequency to the electron plasma frequency, Ω_{ce}/ω_{pe}, was set to 0.1.

Figure 1 shows the three-dimensional simulation model used in this study. In the simulation domain, the grid size dr corresponds to λ_D, where λ_D denotes the Debye length in the plasma flow. The time increment dt was chosen to satisfy the Courant condition, $dr/dt > 1.73v_c$, in three dimensions. As shown in Figure 1a, the number of the grid points in the simulation domain is $192 \times 192 \times 192$. The length of each side of the domain is approximately 5.6L. The electromagnetic perturbation propagating out of the simulation region is attenuated in the absorbing region that encircles the outer boundary; the width of this region is 32 cells. The lunar surface was 5.4L from the left boundary of the simulation region. The coordinate origin was placed at the center of the lunar surface, as shown in Figure 1a.

The upstream plasma was initialized uniformly with v_{flow}, and fresh plasma was continually injected from the left boundary of the simulation region along the positive x direction, which is the antisunward direction. We set B_0 to be along the positive z direction. For the upstream plasma flow, a convective electric field E_0 was introduced along the positive y direction so that condition $E_0 = -v_{flow} \times B_0$ was satisfied in the simulation domain. We did not consider particles which have crossed the lunar surface or other simulation boundaries. At the lunar surface, these particle velocities are counted as the electric current, and they are used to update the normal component of the electric field. Note that the electric field at the lunar surface corresponds to the surface charge, and for simplicity, we assume no photoelectron emissions from the surface.

To show the configuration of the dipole field and each region in the simulation domain, we show two planes which are cut from the region shown in Figure 1a. Figure 1b shows the plane for which $y = 0$. On this plane, we set a magnetic moment $\boldsymbol{M}$ along the positive z direction and at a distance of 0.2L under the lunar surface. The value of $\boldsymbol{M}$ is determined such that $r_{iL}/L = 4$ at a distance of L from the dipole center. Using equation (3) and the parameters of the solar wind and the Reiner Gamma anomaly shown in Table 1, we obtain $L = 32$ km, and r_{iL} at L is approximately 120 km. This implies that r_{iL} is approximately 4 times as large as L, which nearly agrees with the simulation parameter $r_{iL}/L = 4$. The dipole magnetic field and B_0 are considered in the equation of motion when the velocity of each particle is updated. Maxwell's equations are used to determine the variation of the magnetic field. Hereafter, the positive and negative z regions will be referred to as the +M and −M hemispheres, respectively, as shown in Figure 1b.

Figure 1c shows the $z = 0$ plane, which corresponds to the magnetic equator. For convenience, we define the regions of positive and negative y as the +E and −E hemispheres, respectively.

We ran the simulation until the spatial variation of the plasma density reached a steady state.

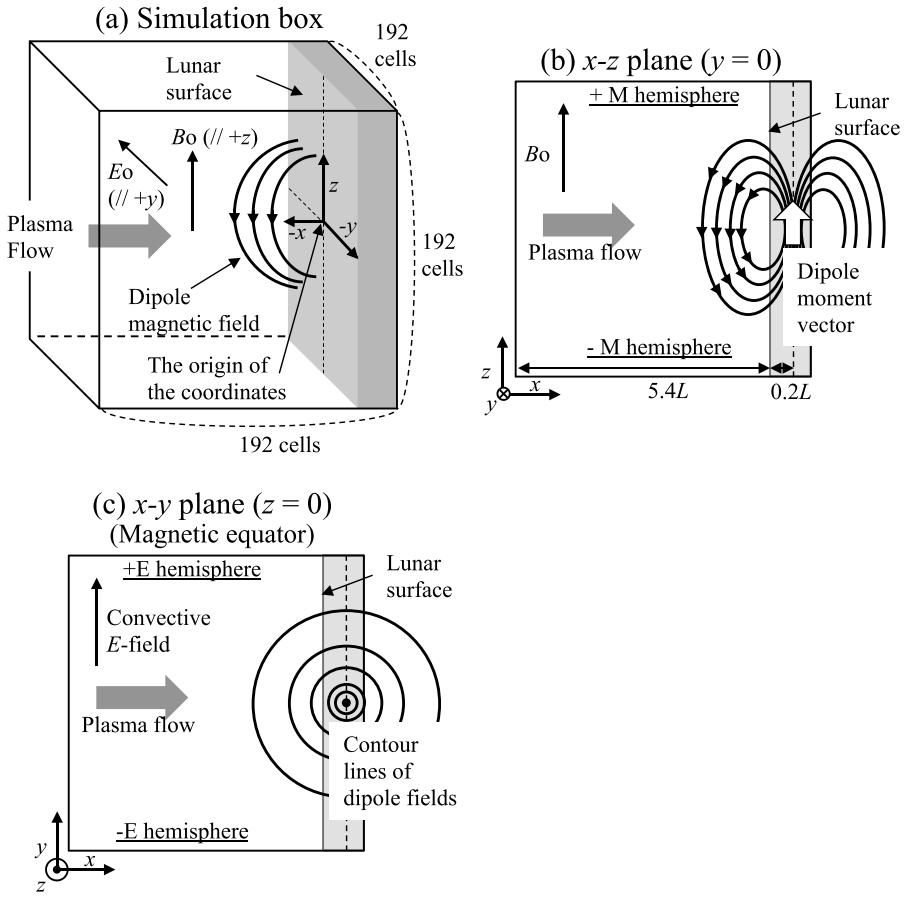

Figure 1. (a) Three-dimensional simulation model, (b) *x*-*z* plane, and (c) *x*-*y* plane.

3. Simulation Results

We examined the density profiles to see if a minimagnetosphere was created by the interaction of the plasma flow with the magnetic anomaly. Figure 2 shows contour maps of the number density of electrons and ions and the charge density obtained at the steady state in the meridian plane, which includes $y/L = 0$. Note that $x/L = 0$ represents the lunar surface, and the coordinate origin is located at the center of the lunar surface. The plasma flows from the left boundary of the simulation domain and along the x direction. The absolute value of x coordinate is the altitude from the lunar surface. In Figure 2, as a reference, we also show some of the field lines (in white) that originate from the dipole moment. The intensities of the magnetic field at representative points along the line $y/L = z/L = 0$ are $|B|/B_0 = 4.3$, 18, and 70 at $x/L = -1.0, -0.5$, and -0.25, respectively. As shown in Figures 2a and 2b, a minimagnetosphere with a plasma cavity is clearly created above the magnetic anomaly; this has been shown in previous studies [e.g., *Harnett and Winglee*, 2000, 2003; *Halekas et al.*, 2008; *Bamford et al.*, 2012]. Figure 2a shows the electron density profile, and it can be seen that the boundary of the minimagnetosphere is curved; this approximately corresponds to the dipole field structure, which is shown in white. It can also be seen that there is a sharp transition to the electron cavity region at the boundary of the magnetosphere; for example, the density transition occurs at $-x/L = 0.3$ along the line $z/L = 0$. We can also see that the density becomes relatively high in the high-latitude regions around $|z|/L = 0.8$ between the lunar surface and $-x/L = 0.3$. These regions correspond to the cusps at which the dipole fields converge to the poles. In Figure 2b, which shows the ion density, we can confirm the formation of a minimagnetosphere similar to the one shown in Figure 2a for electrons. However, the density gradient at the boundary of this minimagnetosphere is not as high as that of the one for the electrons. Because of their large inertia, some ions cross the line of the density transition seen in Figure 2a and reach the inner magnetosphere. In addition, the minimagnetosphere itself seems compressed toward the lunar surface. The ion density becomes relatively high in the high-latitude regions, in which there is a high density of electrons. The spatial profiles of the minimagnetospheres seen in Figures 2a and 2b are similar; however, because of

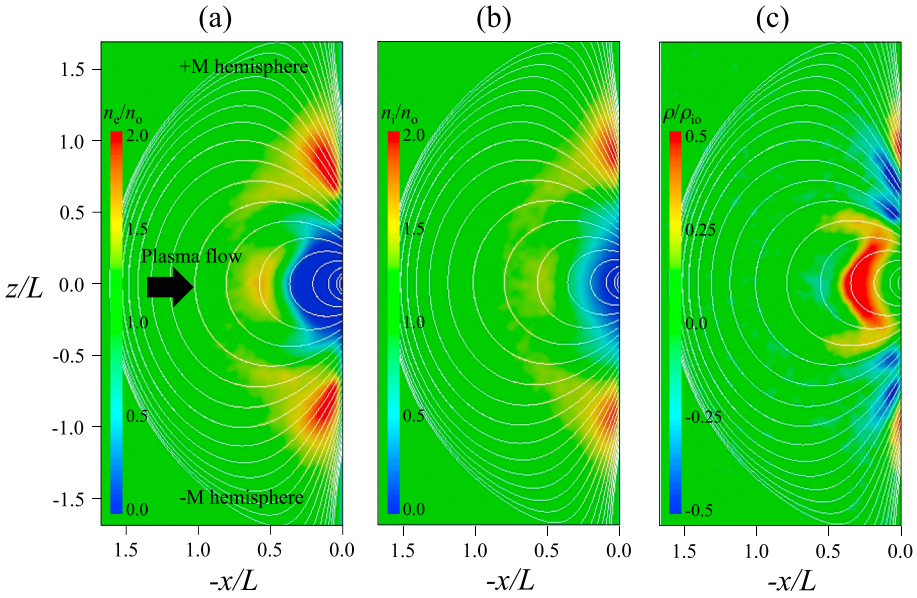

Figure 2. Contour maps of (a) electron density, (b) ion density, and (c) charge density obtained on the meridian plane $y/L = 0$ at the steady state. The densities are normalized to those in the unperturbed upstream plasma flow.

the differences in the density profiles, as discussed above, there is a spatial variation in the charge density, as shown in Figure 2c. As can be seen, the ion density is highest near the magnetic equator and within $|z|/L = 0.5$; this region is shown in red. However, near the lunar surface in both the hemispheres, in the high-latitude regions between $|z|/L \sim 0.5$ and 1.0, the electron density is relatively high; this region is shown in blue. In the vicinity of the lunar surface $x/L = 0$ and around $|z|/L = 1.0$, we also see red regions, indicating that the ion density is high. The density profiles in the vicinity of the lunar surface will be further discussed below.

Figure 3 shows contour maps of the number density of electrons and ions and the charge density at the magnetic equator $z/L = 0$, as in Figure 2. One of the interesting features is that the density profiles in the boundary layer of the minimagnetosphere are asymmetric with respect to the line $y/L = 0$. As shown in Figures 3a and 3b, a high-density region is created for both electrons and ions in the upper region, which corresponds to the +E hemisphere. The profile of the charge density shown in Figure 3c is similar to that shown in Figure 2c. Since ions, which have a larger inertia than do electrons, can reach the inner magnetosphere, the region with a high density of ions (shown in red) is primarily located along the inner boundary of the minimagnetosphere. Like the profiles shown in Figures 3a and 3b, the charge density profile shown in Figure 3c is asymmetric. In the +E hemisphere around $y/L = 0.5$ to 1.0; however, the region with a high density of electrons (shown in blue) is close to the lunar surface. These plasma responses to a magnetic anomaly, including the formation of a minimagnetosphere and the asymmetry of the plasma density, have been investigated in previous studies, and the charge separation at the boundary of the minimagnetosphere has also been discussed [e.g., *Harnett and Winglee*, 2002; *Kallio et al.*, 2012; *Poppe et al.*, 2012; *Deca et al.*, 2014, 2015]. These features are confirmed in our simulation results.

In this study, we are interested in the structure of the boundary layer current of the minimagnetosphere. In Figure 4, we show the vectors of the current density in a three-dimensional region covered with $|y|/L = 1.68$ and $|z|/L = 1.68$ and from the lunar surface up to a height of $x/L = -1.68$. The plot is identical to an all-sky view of the current vectors measured from the coordinate origin on the lunar surface. The current density values are normalized to the ion current density $J_{0i} = qn_0v_{flow}$ in the unperturbed plasma flow, where q denotes the ion charge. The vectors in red indicate where the current density is approximately 4 times J_{0i}. As shown in the +M and −M hemispheres in the figure, the rotational current forms two large structures that are symmetric with respect to the magnetic equator $z/L = 0$. Near the magnetic equator, the current is strongest (shown in red) from the −E to the +E hemisphere. However, in the high-latitude regions, where $|z|/L$ is larger than approximately 0.5, the current density vectors tend to change direction to that seen in the −E hemisphere. The change occurs in the counterclockwise direction in the +M hemisphere and in the clockwise direction in

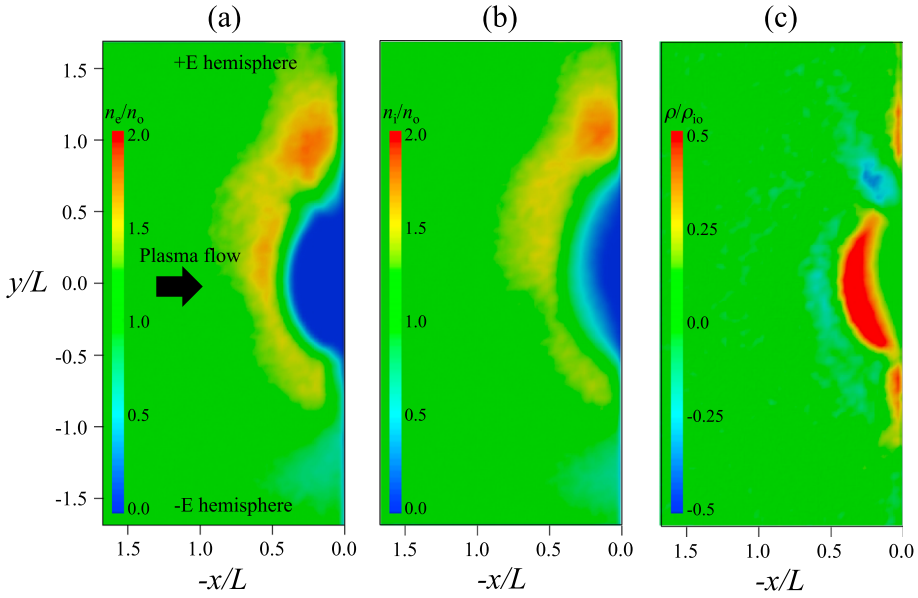

Figure 3. Contour maps of (a) electron density, (b) ion density, and (c) charge density obtained at the magnetic equator $z/L = 0$ at the steady state. The densities are normalized to those in the unperturbed upstream plasma flow.

the −M hemisphere. In other words, the current on the magnetic equator flowing in the direction of the +E hemisphere splits, and each component then turns toward the +M and −M hemispheres.

To examine the boundary layer current in detail, we decompose the current into electron and ion components, as shown in Figure 5. Figure 5 (top and bottom) shows the y component of the current intensity as measured along $y/L = z/L = 0$ on the magnetic equator and $y/L = 0, z/L = 1.0$ in the +M hemisphere, respectively. The electron and ion current densities normalized to J_{0i} are indicated in red and black, respectively. As shown in both panels, the ion current is much smaller than that of the electrons. This implies that the electron current is dominant in the boundary layer. In Figure 5 (top), the current has a peak positive value around $x/L = -0.4$.

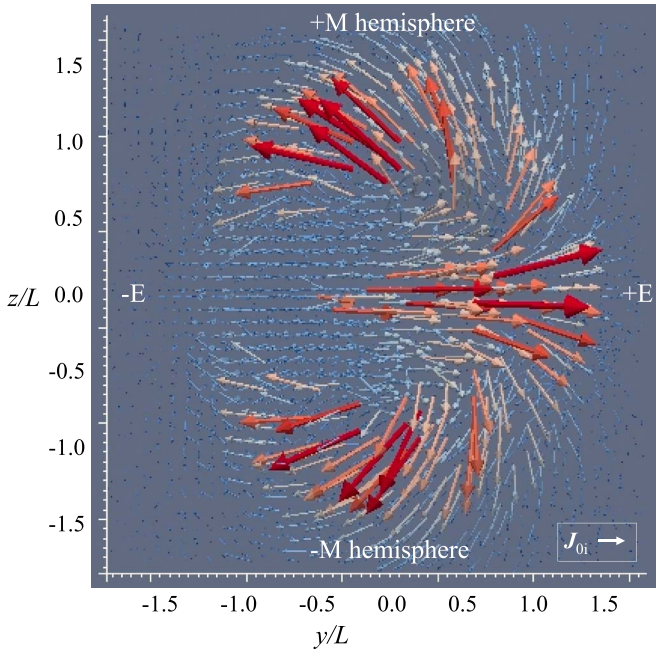

Figure 4. Vectors of current density in a three-dimensional region covered with $|y|/L = 1.68$ and $|z|/L = 1.68$ from the lunar surface up to a height of $x/L = -1.68$.

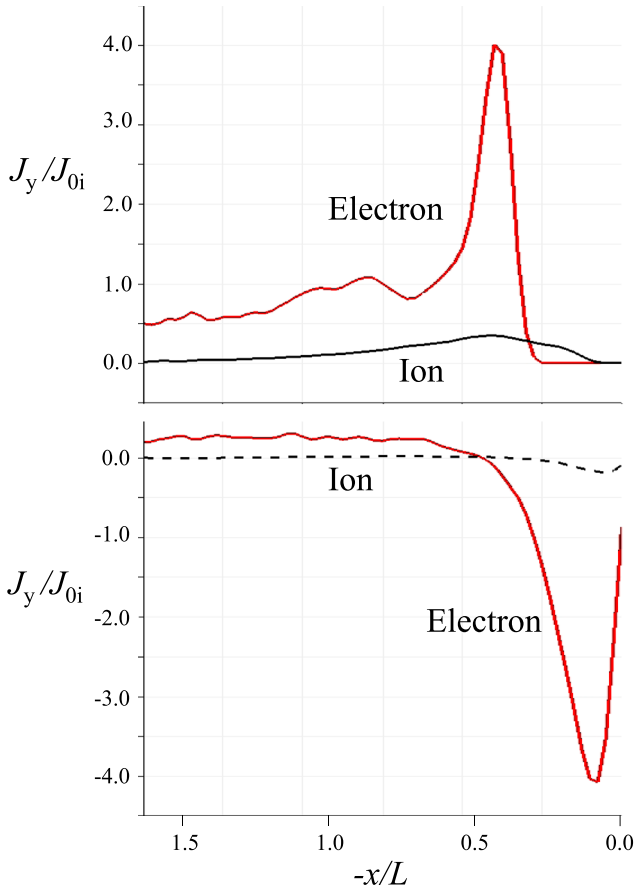

Figure 5. The y components of the electron and ion current densities are plotted along (top) $y/L = z/L = 0$ and (bottom) $y/L = 0, z/L = 1.0$. The current density is normalized to the ion current density J_{0i} in the unperturbed upstream plasma flow.

We note that because electrons have a negative charge, the electron flux points in the negative y direction, which is from the +E to the −E hemisphere. On the other hand, in Figure 5 (bottom), the current has a peak negative value at around $x/L = -0.1$, which is close to the lunar surface. In this case, the direction of the electron flux is toward the +E hemisphere. As can be seen in Figure 5 (top and bottom), the boundary layer is dominated by the electron current, and the electron flux is toward the −E hemisphere at the magnetic equator, while it is toward the +E hemisphere at high latitudes, such as around $z/L = 1.0$ in the +M hemisphere. These signatures of the electron flux agree with the turnaround current structure seen in the three-dimensional space shown in Figure 4. To understand the structure of the boundary layer current, we now consider the electron flux in different planes.

Figure 6 shows vectors of the electron flux in different planes, and these are normalized to that of an ion in the unperturbed upstream flow. In each panel, the color map shown beneath the vectors indicates the electron density. Figures 6a and 6b show the profile at the magnetic equator $z/L = 0$ and at the plane $z/L = 1.0$, respectively. Note that the direction of the vectors in Figure 6 is different from that in Figure 4 because we show the electron flux and not the electron current. In Figure 6a, we see that the electron flux is asymmetric with respect to the line of $y/L = 0$. The electrons enter the +E hemisphere and then stream along the boundary of the magnetosphere toward the −E hemisphere. It is interesting that the intense flux is found inside the region of peak density of electrons in the boundary region. In Figure 6b, we also see a region of intense flux close to the lunar surface. It should be noted that the direction of the flux is the opposite of that seen in Figure 6a; it points to the +E hemisphere.

Figure 6c shows the y-z components of the electron flux vectors in the plane $x/L = -0.1$, superimposed on the electron density color map of the corresponding plane. The panel corresponds to a cross-section of the minimagnetosphere, parallel to the lunar surface. The color map indicates an asymmetric density cavity

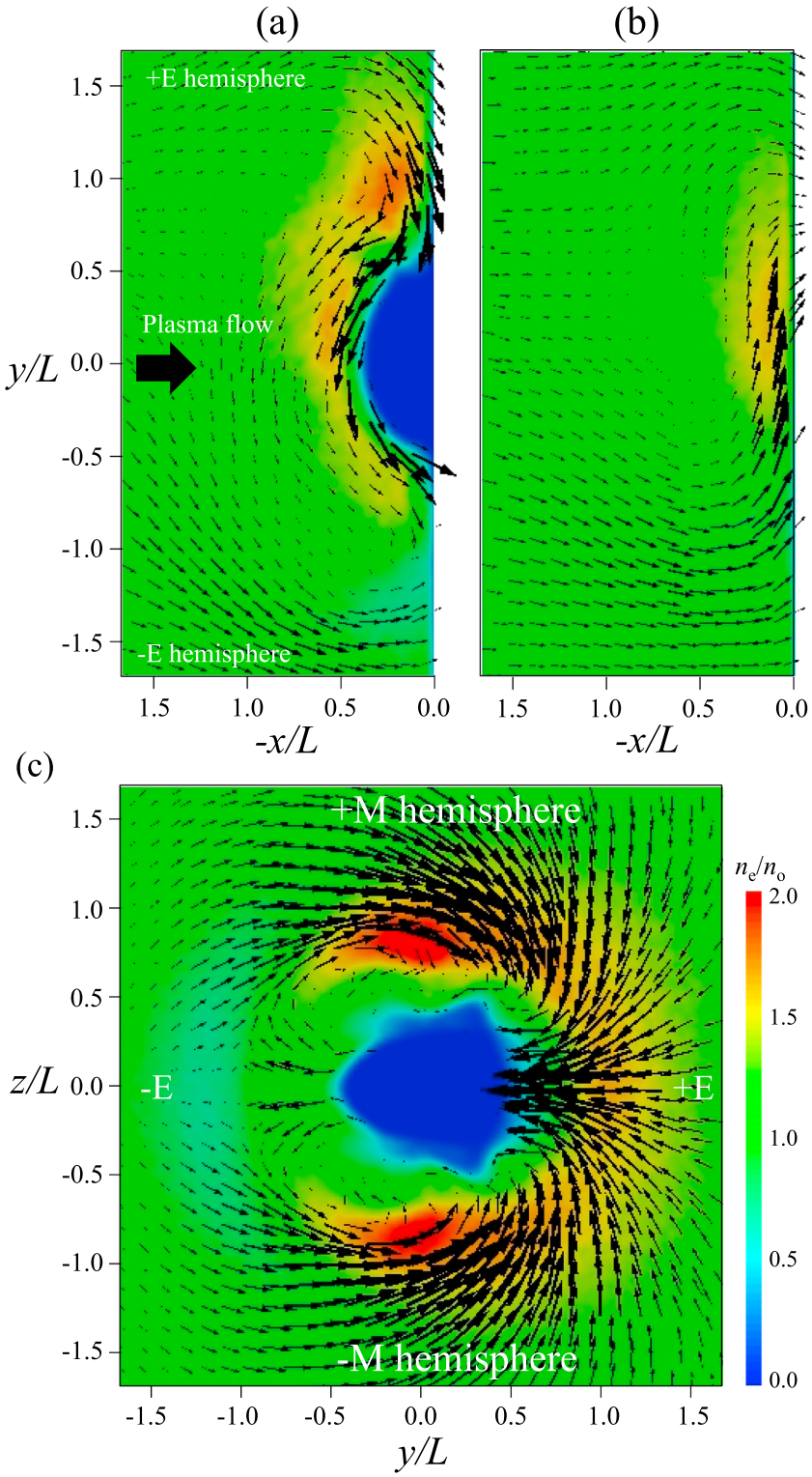

Figure 6. Vectors of electron flux superimposed on the color map of the electron density in the planes of (a) $z/L = 0$, (b) $z/L = 1.0$, and (c) $x/L = 0.1$. The vectors are normalized to the ion flux in the unperturbed upstream flow. For example, in Figure 6a, the maximum vector shown at $x/L = 0.4, y/L = 0.0$ corresponds to a flux that is 4 times the unperturbed ion flux.

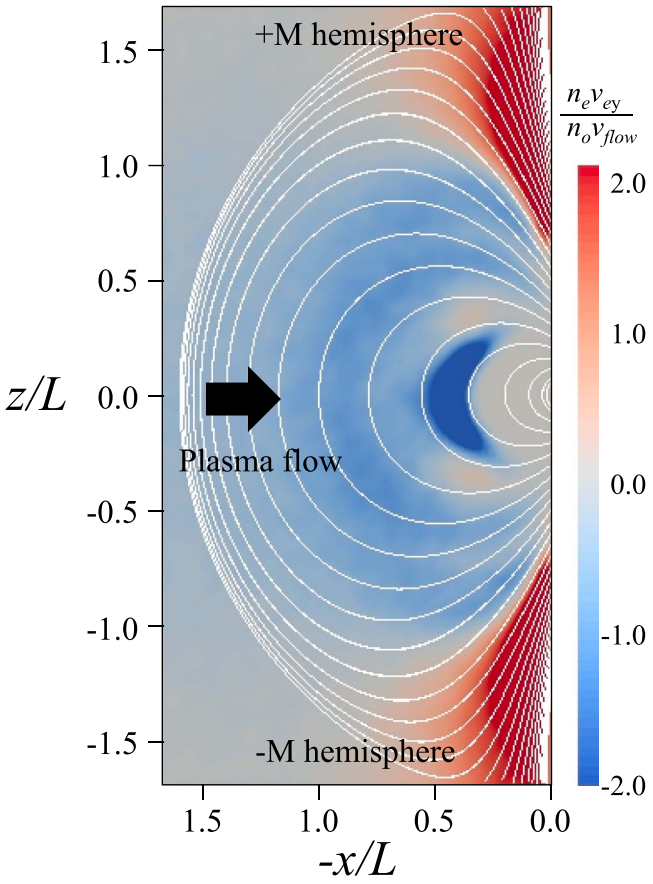

Figure 7. Contour map of the y component of the electron flux on the meridian plane $y/L = 0$. The flux is normalized to the ion flux $n_0 v_{\mathrm{flow}}$ in the unperturbed upstream plasma flow. Some magnetic field lines are plotted on the contour map as a reference.

surrounded by a high-density boundary layer which is also asymmetric. These asymmetric density profiles were also discussed in previous studies [*Deca et al.*, 2014]. As shown in Figure 6c, a large convective structure of electron flux is found in the high-density region of the +M and −M hemispheres. The electron flux shown in Figure 6c seems to turn in the clockwise direction in the +M hemisphere and the counterclockwise direction in the −M hemisphere, the opposite of what was seen for the current vectors in Figure 4. Although not shown in Figure 6c, the electron flux converging to the magnetic equator in the +E hemisphere flows along the inner edge of the boundary layer, as shown in Figure 6a. The flux profiles shown in Figures 6a–6c indicate that electrons flowing to the boundary layer in the +M hemisphere of the minimagnetosphere curve toward the +E hemisphere near the lunar surface and converge to the magnetic equator region; the flow then changes direction and moves toward the −E magnetosphere along the inner boundary layer at the magnetic equator. Electrons flowing to the −M hemisphere show the same behavior as in the +M hemisphere. This three-dimensional profile of the electron flux is in basic agreement with the all-sky view of the current density vectors shown in Figure 4.

To show the dependency of the direction of the electron flux on the distance from the magnetic equator, in Figure 7, we show a contour map for the y component of the electron flux in the $y/L = 0$ plane. As shown in the figure, positive values, which imply that the electron flux is toward the +E hemisphere, are found in the regions of approximately $|z/L| > 0.6$ near the lunar surface in both the +M and −M hemispheres. In other regions, negative values are dominant, as shown in blue, which implies that the electron flux is mostly toward the −E hemisphere. The most intense flux is found around $x/L = -0.4$ at the magnetic equator. We can confirm that because the electron flux is in opposite directions at different distances from the magnetic equator, this results in the turnaround structures seen in both the +M and −M hemispheres, as shown in the current vector profiles in Figure 4.

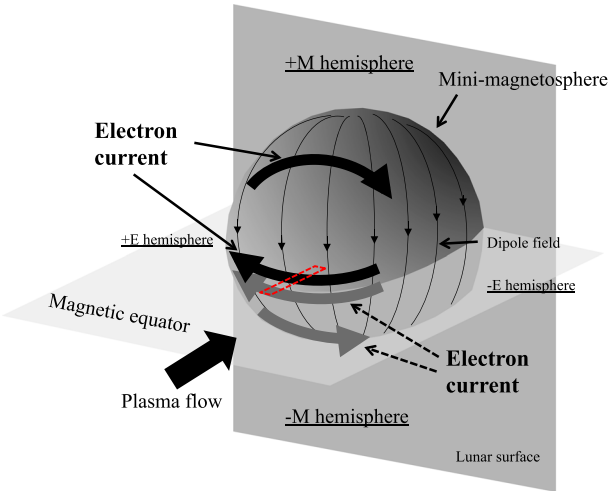

Figure 8. Schematic illustration of the overall pattern of the boundary layer current. Symmetric convection of electron current is seen in the +M and −M hemispheres.

4. Discussion

From the electron flux patterns in different planes, as discussed in the previous section, we can sketch an overall pattern of the boundary layer current in a minimagnetosphere, as shown in Figure 8.

A remarkable feature is the major structures of turnaround convection of electron current that are created in the +M and −M hemispheres; these structures are symmetric with respect to the magnetic equator. Below, we will present a detailed analysis of the electron motion in the boundary layer in the small region indicated by the red dashed line in Figure 8.

As shown in the previous section, we found that the boundary layer current of the minimagnetosphere mainly consists of the electron flux from the +E hemisphere to the −E hemisphere, as shown in Figure 7. When r_{eL} is much smaller than the structure of the minimagnetosphere, as in the present case, the electron flux perpendicular to the dipole field is generally considered to be due to electron drift. In the following discussion, we will consider the electron dynamics in the boundary layer region surrounded by the red dashed line in Figure 8.

In Figure 9a, we show one-dimensional plots of the x component of the electric field E_x and electron and ion densities measured along the line $y/L = z/L = 0$. E_x and the densities are normalized to $v_{flow}B_0$ and n_0, respectively. These quantities are plotted in the region from $x/L = -0.65$ to -0.35, corresponding to the inner boundary layer, where the plasma density starts decreasing toward the lunar surface. As shown in black in Figure 9a, E_x has large negative values, with a peak near $x/L = -0.42$. This intense electric field is caused by the difference in density of electrons and ions in the boundary layer. In particular, between $x/L = -0.5$ and -0.35, the electron density (shown in red) decreases, and the ion density (shown in blue) becomes dominant. Since ions are less magnetized than electrons in the dipole field region, ions can approach the lunar surface closer than can the electrons. The resulting E_x above the magnetic anomaly points in the sunward direction. Note that the dipole magnetic field points toward the −M hemisphere and is perpendicular to the magnetic equator, and thus the $\boldsymbol{E} \times \boldsymbol{B}$ velocity is from the +E hemisphere to the −E hemisphere.

We now consider if the intense electron flux observed at the magnetic equator, as shown in Figure 7, can be explained by the $\boldsymbol{E} \times \boldsymbol{B}$ electron drift. We will consider the v_y component of the motion of electrons along the line $y/L = z/L = 0$. We will assume that the electrons located in the boundary layer are almost magnetized and that r_{eL} is sufficiently small relative to the structure of the boundary layer. Then we can use the following fluid equation for the electrons:

$$m_e n_e \frac{d\boldsymbol{v_e}}{dt} = q_e n_e (\boldsymbol{E} + \boldsymbol{v_e} \times \boldsymbol{B}) - \nabla P_e \tag{4}$$

where v_e and P_e denote the electron velocity and pressure, respectively. Note that because of the fluid approximation, equation (4) does not include the effect of the finite Larmor radius of the ECM. In the above equation,

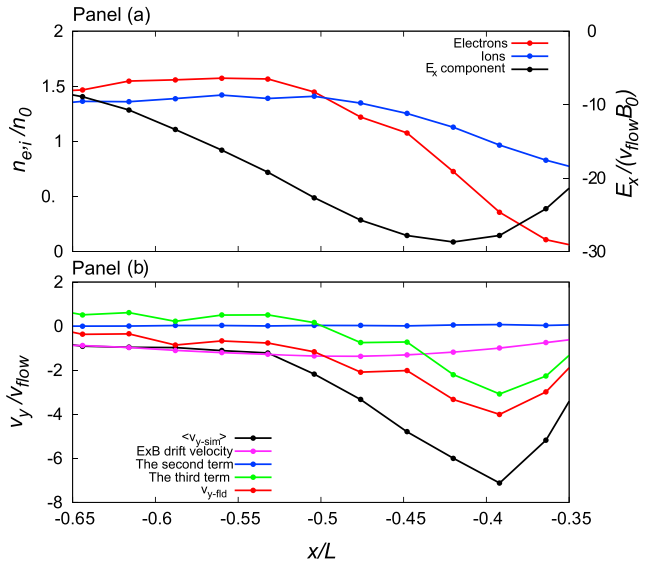

Figure 9. (a) As obtained in the simulation, electron and ion density variation and E_x intensity are plotted in red, blue, and black, respectively, along $y/L = z/L = 0$ in the region between $x/L = -0.65$ and -0.35. (b) The theoretical estimate using equation (6) compared to $< v_{y\text{-sim}} >$, which denotes the average y component of the electron velocity of individual electrons in the simulation. Black, magenta, blue, green, and red curves correspond to $< v_{y\text{-sim}} >$, $E \times B$ drift velocity obtained with the field values in the simulation, the second and third terms in equation (6), and $v_{y\text{-fld}}$ estimated with equation (6), which corresponds to the sum of all the terms in the equation.

if we assume the steady state, $\partial v_e/\partial t = 0$, we obtain the following equation for the x component of the electron velocity v_x:

$$m_e n_e v_x \frac{\partial v_x}{\partial x} = q_e n_e (E_x + v_y B_z) - \frac{\partial P_e}{\partial x} \tag{5}$$

Equation (5) shows the electron forces in the x direction, which corresponds to the plasma flow direction [*Moritaka et al.*, 2012]. From this relation, we can obtain the y component of the electron velocity v_y, as follows (to distinguish this from the simulation result, we will denote it by $v_{y\text{-fld}}$):

$$v_{y\text{-fld}} = -\frac{E_x}{B_z} + \frac{m_e}{q_e B_z} v_x \frac{\partial v_x}{\partial x} + \frac{1}{q_e n_e B_z} \frac{\partial P_e}{\partial x} \tag{6}$$

In equation (6), the first term is the $\boldsymbol{E}\times\boldsymbol{B}$ velocity, the second term is the inertial effect, and the third term is the velocity caused by the spatial variation of the plasma pressure. By using the simulation data for B_z, E_x, n_e, and v_x obtained at each grid point along $y/L = z/L = 0$, we can use equation (6) to estimate $v_{y\text{-fld}}$. In Figure 9b, the first, second, and third terms of equation (6) are plotted in magenta, blue, and green, respectively. The sum of the three terms, which corresponds to $v_{y\text{-fld}}$, is shown in red. The second term, which is the inertial term shown in blue, is negligible in comparison with the other terms. Thus, $v_{y\text{-fld}}$ as estimated with equation (6) is dominated by the first and third terms, which are the $\boldsymbol{E} \times \boldsymbol{B}$ drift velocity and the diamagnetic velocity, respectively. For a comparison, we plotted the simulation results (in black), which were obtained using the average of the v_y component of the individual electrons located at each x position along $y/L = z/L = 0$ in the region indicated by the red dashed line shown in Figure 8, and we will denote these results by $< v_{y\text{-sim}} >$.

In the region between $x/L = -0.65$ and -0.5, the black, red, and magenta curves are in approximate agreement. This implies that $< v_{y\text{-sim}} >$ in this region is mainly due to the $\boldsymbol{E}\times\boldsymbol{B}$ drift velocity (shown in magenta), and thus it can be estimated with fluid theory. The term for the diamagnetic velocity (shown in green) is almost 0 in this region.

In the inner boundary layer between $x/L = -0.5$ and -0.35, however, $< v_{y\text{-sim}} >$ (shown in black) does not match $v_{y\text{-fld}}$ (shown in red). In particular, the difference between it and the $\boldsymbol{E} \times \boldsymbol{B}$ drift velocity (shown in magenta) becomes large. While $< v_{y\text{-sim}} >$ (shown in black) decreases, the $\boldsymbol{E} \times \boldsymbol{B}$ drift velocity (in magenta) maintains almost the same value. As shown in Figure 9a, the intensity of E_x becomes large in the corresponding region, and the $\boldsymbol{E}\times\boldsymbol{B}$ drift velocity is also assumed to increase. However, simultaneously, the dipole magnetic

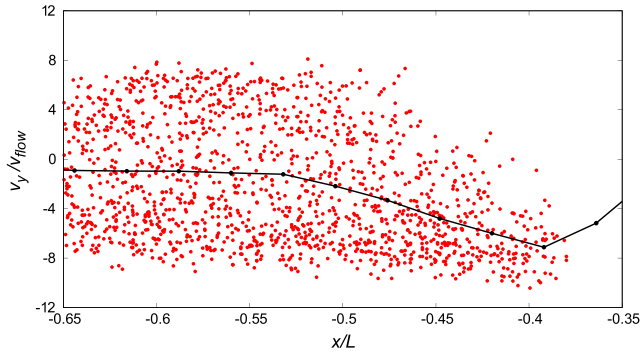

Figure 10. Electron phase diagram in the x-v_y space in the region between $x/L = -0.65$ and -0.35, obtained at the steady state. The velocity is normalized to v_{flow}.

field becomes intense in the same region, and eventually the $\boldsymbol{E} \times \boldsymbol{B}$ drift velocity takes almost the same values (shown in magenta). On the other hand, $v_{y\text{-fld}}$ (shown in red) shows a tendency similar to that of $< v_{y\text{-sim}} >$ (in black). Although these do not match quantitatively, they are qualitatively the same: v_y begins to decrease in this region. Under the fluid approximation, this implies that v_y is dominated by the diamagnetic velocity, which is defined by the third term in equation (6), in the region between $x/L = -0.5$ and -0.4, where the electron density starts to decrease to 0.

Nevertheless, there still exists a quantitative difference between $v_{y\text{-fld}}$ (in red) and $< v_{y\text{-sim}} >$ (in black).

In order to understand this difference, we consider the finite Larmor radius of the ECM. In Figure 10, we plot the v_y component of individual electrons (red dots) located in the region indicated by the red dashed line shown in Figure 8 along the line $y/L = z/L = 0$. The velocity values are normalized to v_{flow}. As a reference, we superimpose the average v_y, which is the same as $< v_{y\text{-sim}} >$ shown in the previous figure.

As is clearly shown, the electrons are uniformly distributed in the region between $x/L = -0.65$ and -0.5. However, in the region between $x/L = -0.5$ and -0.4, the velocity distribution starts to converge, and the center of the distribution decreases down to $v_y/v_{flow} = -8$. It should be noted that electrons located in the region between $x/L = -0.65$ and -0.5 are distributed on the v_y axis with a velocity range that is much larger than v_{the} of the unperturbed plasma flow. In addition, it is very interesting to note that electrons in the region between $x/L = -0.5$ and -0.4 have no positive v_y. The above mentioned features of the electron distribution are closely associated with the ECM and are directly reflected in the curve of $< v_{y\text{-sim}} >$ (shown in black).

To see the ECM effect on the electron velocity distribution in the boundary layer, we plotted individual electrons in the v_x-v_y phase space for different regions along $y/L = z/L = 0$, as shown in Figure 11. Since the dipole magnetic field is perpendicular to the magnetic equator, the ECM is directly mapped in the v_x-v_y phase space.

Figure 11a shows the region of unperturbed plasma flow, while the other panels show different regions in the boundary layer between $x/L = -0.6$ and -0.4. Figure 11a shows the unperturbed Maxwellian velocity distribution of the electrons which have drift velocity of v_{flow} in the positive x direction. When these electrons enter the boundary layer, they begin gyrating in the dipole magnetic field and are affected by the electric field caused by the charge separation shown in black in Figure 9a. In Figure 11b, we show a phase plot of the electrons located between $x/L = -0.59$ and -0.53. It can be clearly seen that the electrons accelerated by E_x form a gyrotropic ring distribution in the v_x-v_y phase space. The maximum velocity of these electrons is approximately $|v|/v_{flow} = 8$, which is much larger than the ambient thermal velocity $v_{the}/v_{flow} = 2.4$. Although the MHD approximation for electrons breaks in this region, $< v_{y\text{-sim}} >$ agrees well with the $\boldsymbol{E} \times \boldsymbol{B}$ velocity because the electrons are gyrotropically distributed in the v_x-v_y phase space.

Figure 11c shows a phase plot for the electrons located in the boundary layer closer to the lunar surface, between $x/L = -0.48$ and -0.42, where the electron density starts to decrease. It should be stressed that the upper half of the velocity distribution is almost missing in Figure 11c. This nonuniform distribution agrees with the absence of electrons with positive v_y in the region $x/L > -0.5$, as shown in Figure 10. In this region, the electron density decreases in the antisunward direction because the intensity of the local magnetic field becomes large. Assuming that the Larmor radius of the accelerated electrons is larger than the

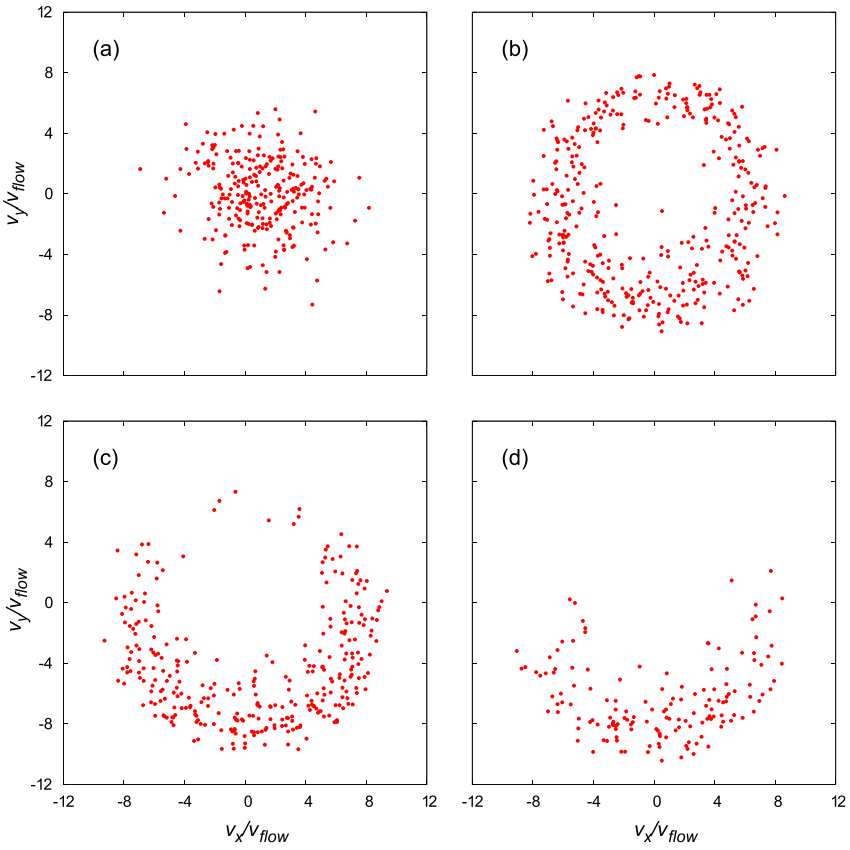

Figure 11. Electron phase diagrams in the v_x-v_y space in (a) the unperturbed region at $x/L = -5.0$, (b) the region between $x/L = -0.59$ and -0.53, (c) the region between $x/L = -0.48$ and -0.42, and (d) the region between $x/L = -0.42$ and -0.36.

region presented in Figure 11c, electrons in the gyration phase with a positive v_y are spatially filtered out of the plot region, and only the electrons with a negative v_y component (from the +E hemisphere to the −E hemisphere) remain.

In Figure 11d, we show another phase plot of the electrons located between $x/L = -0.42$ and -0.36. As shown in the panel, most of the electrons have the maximum negative v_y component with $|v|/v_{\mathrm{flow}} = 8$. This implies that due to the finite Larmor radius of the ECM, most of the electrons located at the innermost edge of the boundary layer are pointing toward the −E hemisphere.

According to the previous studies that have used PIC simulations [e.g., *Deca et al.*, 2014], the electron current at the minimagnetosphere boundary is simply due to the $\boldsymbol{E} \times \boldsymbol{B}$ electron drift. This is true for the macroscopic behavior of electrons in the boundary layer region. However, we found that the maximum electron velocity observed at the innermost edge of the boundary layer as shown in Figure 11d does not agree with that of the conventional $\boldsymbol{E} \times \boldsymbol{B}$ drift. Considering the finite Larmor radius of the ECM, we clarified that the maximum velocity of the electrons was due to the acceleration by the electric field in the boundary layer. This is one of the most significant findings in this study.

Although the intensity of the dipole magnetic field changes depending on the distance from the lunar surface, the average intensity is approximately $|B|/B_0 = 20$ in the inner boundary layer between $x/L = -0.5$ and -0.4. Assuming that the averaged velocity of the accelerated electrons is $|v|/v_{\mathrm{flow}} = 8$, as shown in Figure 11d, we can estimate that r_{eL} becomes approximately $0.08L$. This radius is in approximate agreement with the distance between $x/L = -0.5$ and -0.4, where the electron density gradually decreases to 0. In other words, the width of the inner boundary layer with the intense electron flux is approximately equivalent to the radius of the local ECM, which is not related to the ion dynamics. This is another significant finding of the present study.

We will now quantitatively evaluate the electron acceleration of $|v|/v_{flow} = 8$, which is shown in Figure 11. The following is a rough estimate of the electron acceleration in the inner boundary layer. As we noted previously, E_x is enhanced by the charge separation in the inner boundary layer and in the sunward direction. The electrons entering this region are accelerated by this E_x. The kinetic energy gained by these electrons is equal to the potential energy created in the corresponding region. When we focus on the region between $x/L = -0.6$ and -0.4 in Figure 9, the average (normalized) value of E_x is roughly -20. The difference in the electric potential over the region is estimated by multiplying the spatial length of the region, $0.2L$, by the average E_x. By using the estimated potential difference, we can calculate the kinetic energy which the electrons gain as they travel in this region. Note that the spatial length of the corresponding region is $0.2L$, which is about the diameter of the electron gyration in the inner boundary layer. For simplicity, we can assume that the electrons can be accelerated along the x direction for a distance of $0.2L$, without much constraint due to the dipole field. From the kinetic energy of the electrons calculated above, the gained velocity is approximated as $6.3v_{flow}$. This rough estimate of the electron acceleration in the charge separation region is of the same order as the simulation result, which is $|v|/v_{flow} = 8$, as shown in Figure 11b.

From a macroscopic point of view, a question remains about the closure of the current in the boundary layer. In the present simulation, we assumed no emission of photoelectrons from the lunar surface. In addition, there exists no ionosphere in the lunar environment. In such a situation, the boundary current of a minimagnetosphere cannot be closed by the plasma that originates at the lunar surface. Although we have not yet performed a detailed analysis of the current closure in a lunar surface environment, we can imagine that the plasma flux at the boundary of the minimagnetosphere will eventually impinge on the lunar surface and thus contribute to the surface charge.

As shown in Figure 2c, we see high-density regions of electrons at the polar regions around $|z|/L = 0.5$ in the vicinity of the lunar surface. In these regions, the magnetic fields converge, and the incoming electrons concentrate in the cusp-like dipole fields. Eventually, the electron density becomes higher than that of the ions. However, it is difficult for the electrons to enter the region just outside the cusp regions around $|z|/L = 1.0$, where the dipole field becomes almost perpendicular to the plasma flow, and so the density becomes rather small. On the other hand, it is easier for ions in the plasma flow to approach the lunar surface than it is for electrons, since the ions have relatively large inertia. The ion density thus becomes high near the lunar surface. A similar signature is found in the charge density profile at the magnetic equator, as shown in Figure 3c. In the boundary layer regions around $|y|/L = 1.0$, where the densities are high for both species, the charge density becomes positive because the ion density is higher than that of the electrons. This occurs because the large r_{iL} allows the ions to approach the lunar surface. Considering these signatures of the charge density, we note that the surface charging in the region surrounding the plasma cavity of the minimagnetosphere can be positive because the dominant contribution is due to ions impinging on the surface. Since a quantitative analysis of the surface charging is beyond the scope of the current study, we leave it as an area of future work.

In previous studies based on hybrid particle simulation, it has been found that an electric field in the sunward direction is induced above the magnetic anomaly due to the decoupling of electron and ion motion in the boundary layer; this occurs even without separation of charge [*Jarvinen et al.*, 2014; *Fatemi et al.*, 2015]. In the present simulation, the electric field was similarly enhanced in the boundary layer. From an evaluation of these results, it is clear that the significant factor for the enhancement of the electric field is the difference between the motion of electrons and that of ions in the boundary layer; this was simulated in both the full particle and the hybrid models. The charge separation observed in the present simulation was due to the decoupling of the two species of particles in the dipole field.

A unique and significant aspect of the present study is the use of a full particle model that allows the analysis of the electron dynamics by solving for the dynamics of the individual particles. This provides a large advantage over the hybrid and MHD simulations. In particular, as shown in Figures 10 and 11, a full particle simulation allows us to obtain the electron velocity distribution, the acceleration of the electrons by the electric field, and the resulting formation of a ring-like velocity distribution in the boundary layer. These results are new findings which have not been previously presented.

In this study, we assumed that B_0 was uniform and pointed in the positive z direction. Like the Earth's magnetosphere, the orientation of B_0 may affect the shape of the minimagnetosphere due to its interaction with the dipole field. As an area of future work, the orientation of B_0 on the physics of the minimagnetosphere should be examined.

5. Conclusions

We studied the electron dynamics in a minimagnetosphere created above a lunar magnetic anomaly by performing three-dimensional electromagnetic particle-in-cell simulations. In this study, we focused on the following two aspects on the electron current, which dominates in the boundary layer. The first is the three-dimensional structure of the boundary layer current of the minimagnetosphere. The second is the electron cyclotron motion in the boundary layer current, examined at the magnetic equator. The simulations revealed that the profile of the electron boundary current shows turnaround convection structures in the +M and −M hemispheres, and these are symmetric with respect to the magnetic equator. The electrons flowing to +M and −M hemispheres of the minimagnetosphere change direction and head toward the +E hemisphere near the lunar surface; they converge at the magnetic equator. The electron flow then changes direction and heads toward the −E hemisphere, traveling along the inner boundary of the minimagnetosphere on the magnetic equator. The simulations also revealed the mechanism by which the electrons obtain their maximum velocity, which is observed at the edge of the inner boundary layer, where the electron density gradually decreases to 0. We clarified that the maximum electron velocity is due to the acceleration by the electric field, which is enhanced by the charge separation, and it is not simply due to the $\boldsymbol{E}\times\boldsymbol{B}$ drift. Due to the finite Larmor radius of the ECM with the maximum velocity, intense electron current flows at the innermost boundary layer in the magnetic equator. We also confirmed that the width of the boundary current layer is approximately equal to the radius of the local ECM. These simulation results strongly suggest that the ECM and the finite Larmor radius of the electrons are significant for understanding the electron current in the boundary layer of a minimagnetosphere.

As an area of future work, we plan to further study the electron flux in the boundary layer near the polar regions, where the flux direction is opposite that observed at the magnetic equator. Unlike the situation at the magnetic equator, in the polar regions, the direction of the dipole field is not simply perpendicular to the plasma flow. Thus, when the $\boldsymbol{E}\times\boldsymbol{B}$ drift is a major source of electron flux, it is necessary to consider the relative angle between the local E field due to the charge separation and the dipole magnetic field. It is also necessary to consider the finite Larmor radius of the electron in order to examine the electron velocity at the edges of the boundary current in the polar regions.

Acknowledgments
This work was supported by JSPS KAKENHI grant 23340148 and 16H04058. Computation resources have been provided by the KDK of Kyoto University and the π-computer of ECCSE in Kobe University. The data for this paper are available on request; contact H. Usui at h-usui@port.kobe-u.ac.jp.

References

Ashida, Y., H. Usui, I. Shinohara, M. Nakamura, I. Funaki, Y. Miyake, and H. Yamakawa (2014), Full kinetic simulations of plasma flow interactions with meso- and microscale magnetic dipoles, *Phys. Plasmas*, *21*(12), 122903, doi:10.1063/1.4904303.

Bamford, R. A., B. Kellett, W. J. Bradford, C. Norberg, A. Thornton, K. J. Gibson, I. A. Crawford, L. Silva, L. Gargate, and R. Bingham (2012), Minimagnetospheres above the lunar surface and the formation of lunar swirls, *Phys. Rev. Lett.*, *109*, 081101, doi:10.1103/PhysRevLett.109.081101.

Barabash, S., et al. (2009), Investigation of the solar wind-moon interaction onboard chandrayaan-1 mission with the sara experiment, *Curr. Sci.*, *96*(4), 526–532.

Bhardwaj, A., S. Barabash, M. B. Dhanya, M. Wieser, F. Yoshifumi, M. Holmstrom, R. Sridharan, P. Wurz, A. Schaufelberger, and A. Kazushi (2010), Studying the Lunar-Solar Wind Interaction with the SARA Experiment aboard the Indian Lunar Mission Chandrayaan-1, *AIP Conf. Proc.*, *1216*, 518–521, doi:10.1063/1.3395916.

Birdsall, C. K., and A. B. Langdon (1991), *Plasma Physics via Computer Simulation*, Plasma Physics Series, Institute of Physics Publ., England.

Deca, J., A. Divin, G. Lapenta, B. Lembege, S. Markidis, and M. Horanyi (2014), Electromagnetic particle-in-cell simulations of the solar wind interaction with lunar magnetic anomalies, *Phys. Rev. Lett.*, *112*, 151102, doi:10.1103/PhysRevLett.112.151102.

Deca, J., A. Divin, B. Lembege, M. Horanyi, S. Markidis, and G. Lapenta (2015), General mechanism and dynamics of the solar wind interaction with lunar magnetic anomalies from 3-d particle-in-cell simulations, *J. Geophys. Res. Space Physics*, *120*, 6443–6463, doi:10.1002/2015JA021070.

Fatemi, S., C. Lue, M. Holmstrom, A. R. Poppe, M. Wieser, S. Barabash, and G. T. Delory (2015), Solar wind plasma interaction with gerasimovich lunar magnetic anomaly, *J. Geophys. Res. Space Physics*, *120*, 4719–4735, doi:10.1002/2015JA021027.

Halekas, J. S., D. A. Brain, D. L. Mitchell, and R. P. Lin (2006), Whistler waves observed near lunar crustal magnetic sources, *Geophys. Res. Lett.*, *33*, L22104, doi:10.1029/2006GL027684.

Halekas, J. S., G. T. Delory, D. A. Brain, R. P. Lin, and D. L. Mitchell (2008), Density cavity observed over a strong lunar crustal magnetic anomaly in the solar wind: A mini-magneto sphere?, *Planet. Space Sci.*, *56*(7), 941–946, doi:10.1016/j.pss.2008.01.008.

Harnett, E. M., and R. Winglee (2000), Two-dimensional mhd simulation of the solar wind interaction with magnetic field anomalies on the surface of the moon, *J. Geophys. Res.*, *105*(A11), 24,997–25,007, doi:10.1029/2000JA000074.

Harnett, E. M., and R. M. Winglee (2002), 2.5d particle and mhd simulations of mini-magnetospheres at the moon, *J. Geophys. Res.*, *107*(A12), 1421, doi:10.1029/2002JA009241.

Harnett, E. M., and R. M. Winglee (2003), 2.5-D fluid simulations of the solar wind interacting with multiple dipoles on the surface of the moon, *J. Geophys. Res.*, *108*(A2), 1088, doi:10.1029/2002JA009617.

Hashimoto, K., et al. (2010), Electrostatic solitary waves associated with magnetic anomalies and wake boundary of the moon observed by kaguya, *Geophys. Res. Lett.*, *37*, L19204, doi:10.1029/2010GL044529.

Howes, C. T., X. Wang, J. Deca, and M. Horanyi (2015), Laboratory investigation of lunar surface electric potentials in magnetic anomaly regions, *Geophys. Res. Lett.*, *42*, 4280–4287, doi:10.1002/2015GL063943.

Jarvinen, R., M. Alho, E. Kallio, P. Wurz, S. Barabash, and Y. Futaana (2014), On vertical electric fields at lunarmagnetic anomalies, *Geophys. Res. Lett.*, *41*, 2243–2249, doi:10.1002/2014GL059788.

Kallio, E., et al. (2012), Kinetic simulations of finite gyroradius effects in the lunar plasma environment on global, meso, and microscales, *Planet. Space Sci.*, *74*(1), 146–155, doi:10.1016/j.pss.2012.09.012.

Kurata, M., H. Tsunakawa, Y. Saito, H. Shibuya, M. Matsushima, and H. Shimizu (2005), Mini-magnetosphere over the reiner gamma magnetic anomaly region on the moon, *Geophys. Res. Lett.*, *32*, L24205, doi:10.1029/2005GL024097.

Lue, C., Y. Futaana, S. Barabash, M. Wieser, M. Holmstrom, A. Bhardwaj, M. B. Dhanya, and P. Wurz (2011), Strong influence of lunar crustal fields on the solar wind flow, *Geophys. Res. Lett.*, *38*, L03202, doi:10.1029/2010GL046215.

Moritaka, T., Y. Kajimura, H. Usui, M. Matsumoto, T. Matsui, and I. Shinohara (2012), Momentum transfer of solar wind plasma in a kinetic scale magnetosphere, *Phys. Plasmas*, *19*(3), 032111, doi:10.1063/1.3683560.

Poppe, A. R., J. S. Halekas, G. T. Delory, and W. M. Farrell (2012), Particle-in-cell simulations of the solar wind interaction with lunar crustal magnetic anomalies: Magnetic cusp regions, *J. Geophys. Res.*, *117*, A09105, doi:10.1029/2012JA017844.

Saito, Y., et al. (2008), Solar wind proton reflection at the lunar surface: Low energy ion measurement by MAP-PACE onboard SELENE (KAGUYA), *Geophys. Res. Lett.*, *35*, L24205, doi:10.1029/2008GL036077.

Saito, Y., et al. (2010), In-flight performance and initial results of plasma energy angle and composition experiment (PACE) on selene (KAGUYA), *Space Sci. Rev.*, *154*(1–4), 265–303, doi:10.1007/s11214-010-9647-x.

Saito, Y., M. N. Nishino, M. Fujimoto, T. Yamamoto, S. Yokota, H. Tsunakawa, H. Shibuya, M. Matsushima, H. Shimizu, and F. Takahashi (2012), Simultaneous observation of the electron acceleration and ion deceleration over lunar magnetic anomalies, *Earth Planets Space*, *64*(2), 83–92, doi:10.5047/eps.2011.07.011.

Villasenor, J., and O. Buneman (1992), Rigorous charge conservation for local electromagnetic-field solvers, *Comput. Phys. Commun.*, *69*(2–3), 306–316, doi:10.1016/0010-4655(92)90169-y.

Wang, X., C. T. Howes, M. Horanyi, and S. Robertson (2013), Electric potentials in magnetic dipole fields normal and oblique to a surface in plasma: Understanding the solar wind interaction with lunar magnetic anomalies, *Geophys. Res. Lett.*, *40*, 1686–1690, doi:10.1002/grl.50367.

Wieser, M., S. Barabash, Y. Futaana, M. Holmstrom, A. Bhardwaj, R. Sridharan, M. B. Dhanya, A. Schaufelberger, P. Wurz, and K. Asamura (2010), First observation of a mini-magnetosphere above a lunar magnetic anomaly using energetic neutral atoms, *Geophys. Res. Lett.*, *37*, L05103, doi:10.1029/2009GL041721.

Winglee, R. M., J. Slough, T. Ziemba, and A. Goodson (2000), Mini-magnetospheric plasma propulsion: Tapping the energy of the solar wind for spacecraft propulsion, *J. Geophys. Res.*, *105*(A9), 21,067–21,077, doi:10.1029/1999JA000334.